



AEROELASTIC WING ANALYSIS AND DESIGN

Ivo M. D. Rocha¹ and André C. Marta^{2*}

1: Instituto Superior Técnico, Universidade de Lisboa
Av. Rovisco Pais 1, 1049-001 Lisboa, Portugal
e-mail: ivo.rocha@tecnico.ulisboa.pt

2: IDMEC, Instituto Superior Técnico, Universidade de Lisboa
Av. Rovisco Pais 1, 1049-001 Lisboa, Portugal
e-mail: andre.marta@tecnico.ulisboa.pt

Keywords: Aircraft design, flutter, divergence speed, fluid-structure interaction, wind tunnel, optimization

Abstract. *Since the early days of aviation, aeroelastic problems have shown to be some of the most challenging to solve. With the development of numerical methods, the study of aircraft structures and their interaction with the surrounding air flow at different flight conditions has become easily accessible and, thus, is now mandatory in the design phase of an aircraft. This work focuses on the development of a numerical tool for aircraft wing fluid-structure interaction (FSI) analyses, in which the external airflow and the internal structure interact. A panel method was implemented for the aerodynamic analysis and a finite-element model using equivalent beam elements was implemented for the structural analysis, both coded in MATLAB[®] language. Each analysis models were successfully individually verified against other bibliographic sources and then the two disciplines were coupled into the FSI numerical tool. To validate the accuracy of the numerical tool to predict aeroelastic parameters, such as flutter and divergence speeds, a half wing prototype was built and tested in a wind tunnel. The wing shape was parameterized using area, airfoil cross-section shape, aspect ratio, taper ratio, sweep angle and dihedral angle. Before the optimization, a parametric study was conducted to study the influence of these parameters in the wing performance. The validated FSI tool was then used in an optimization framework to obtain an optimized wing shape with the objective of maximizing the lift-to-drag ratio whilst guaranteeing that flutter and divergence behavior are not worse than that of the baseline wing.*

1 INTRODUCTION

Recent developments in wing design, such as active aeroelastic wings [1]), higher aspect ratios (AR) and morphing shapes during flight [2, 3], have furthered the need of reliable

prediction of aeroelastic phenomena, since these new flexible wings can easily lead to aeroelastic instabilities, even inside standard flight envelope conditions. The novel designs are being adopted in Unmanned Air Vehicles (UAV), such as the High Altitude Long Endurance (HALE) Airbus Zephyr in Fig.1, where the very high AR wing decreases induced drag, thus improves the aerodynamic performance.



Figure 1: Airbus Zephyr HALE UAV

Given that small to medium size UAVs fly at relatively low speeds, their aerodynamic behavior can be accurately modeled by low complexity models. However, there is a lack of readily available aeroelastic experimental data for these speed ranges, as most studies are performed at the transonic speeds [4, 5, 6]. There are some attempts to improve data for experimental confirmation, particularly for the case of geometric non-linearities [7] but, for the most part, there is a need for a broad range of aeroelastic testing data cases [8], specially with the recent numerical developments concerning the simulation of geometric non-linear behavior and Limit Cycle Oscillations [9, 10].

Besides the introduction of more complex geometric definitions, there is interest in analyzing several possible interface methods between the aerodynamic and structural models [11] to improve accuracy of current aeroelastic tools. Another advantage of the increased accuracy of aeroelastic tools is the possibility of incorporating optimizing algorithms to their architecture to allow design refining around the expected aeroelastic behavior of an aircraft, that leads to considerable design time savings.

The goals of this work is then to develop an aeroelastic analysis and design framework, capable of handling highly flexible wings, that predicts accurately the wing aeroelastic response, in particular divergence speed and flutter speed.

2 COMPUTATIONAL AEROELASTICITY

Computational Aeroelasticity (CAE) specifically refers to the coupling of Computational Fluid Dynamics (CFD) methods with Computational Structural Dynamics (CSD) tools to perform aeroelastic analyses [5].

The basis for any CAE methodology is the coupled equations of motion,

$$[M]\ddot{\mathbf{q}}(t) + [D]\dot{\mathbf{q}}(t) + [K]\mathbf{q}(t) = \mathbf{F}(t), \quad (1)$$

where M , D and K are generalized mass, damping and stiffness matrices, respectively, $\mathbf{F}(t)$ is generalized force vector that accounts for the aerodynamic loads, and $\mathbf{q}(t)$ is the generalized displacement vector [12]. It is then necessary to model each discipline with CFD and CSD numerical tools, and then provide an adequate coupling between the two.

2.1 Coupling Models

A typical structure of an aeroelastic tool is shown in Fig. 2, where the Fluid-Structure Interface (FSI) is highlighted.

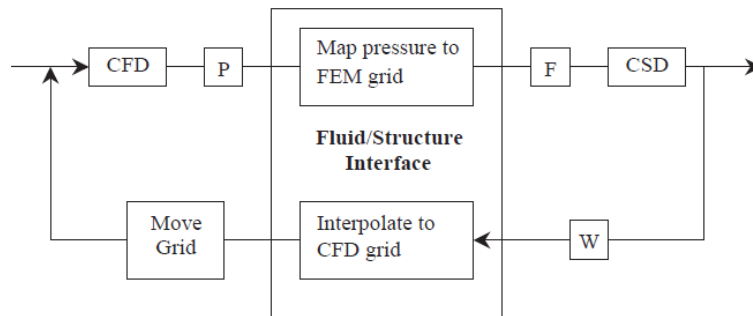


Figure 2: Structure of a typical coupled aeroelastic tool [5]

The FSI is paramount to connecting the separate discipline modules of the aeroelastic framework, and that can be done using a fully-coupled model, a loosely coupled model or a closely coupled model [5]. While the fully coupled FSI integrates and solves the combined fluid and structural equations of motion simultaneously in one single solver, the other two solve then separately using different solvers. The first approach is not only very rigid in terms of choice of discipline models but also usually computationally expensive. In contrast, the loosely and closely coupled models, though requiring an interface to exchange information between aerodynamic and structural solvers and loosing some accuracy, allow the flexibility of choosing different solvers for each discipline [5]. While in the loosely coupled the exchange of information only takes place after partial or complete convergence of each solver, in the closely coupled model the discipline solvers exchange of information at the boundary via an interface module, making the entire CAE model tightly coupled and, thus, with improved accuracy. The information exchanged are surface loads, output of CFD and input to CSD, and surface deformation, output of CSD and input to CFD.

By selecting a loosely coupled or a closely coupled model, it is possible to have two separate solvers for each aerodynamic and structural model computations, both reducing the complexity of implementation and allowing an easier validation of results.

2.2 Discipline models

As far as aerodynamic models go, there are several options to choose, as illustrated in Fig.13(a), depending on the complexity of the flow considered.

Since our aim is to study aeroelastic effects in wings, 3D effects must be accounted for, in particular at the wing tip. However, the driving forces in aeroelasticity are mainly

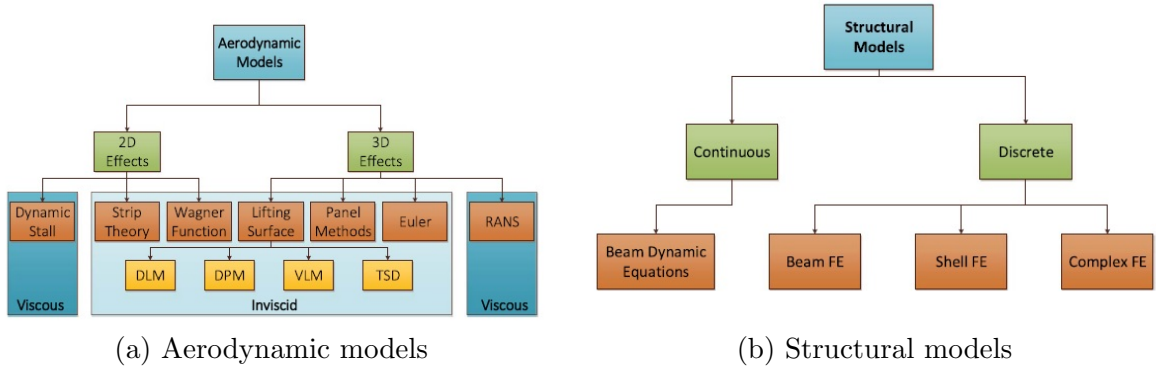


Figure 3: FSI discipline models [13]

inviscid, and the low flow speeds considered in our design cases mean rotational and compressibility effects might be discarded. Given that we want to model the lifting surface thickness, the appropriate models, balancing required complexity and available computational power, are the panel methods[14]. These models are based on potential flow equations and they are relatively easy to implement and integrate in an FSI model.

As for structural models, while it is possible to choose between continuous and discrete models as shown in Fig.13(b), the implementation of discrete models is required to couple it in the FSI tool. Among the different Finite Elements (FE), the beam FE is the simplest model, but accurate enough for low and medium fidelity applications, such as simulating a solid wing or a spar [15].

3 NUMERICAL IMPLEMENTATION

3.1 Aerodynamic Model

The methodology followed to implement the 3D panel method is similar to the defined by Katz [16]. This model is based on the potential flow equation, valid for incompressible, inviscid and irrotational flow,

$$\nabla^2 \Phi^* = 0, \quad (2)$$

where Φ^* is the total velocity potential. Equation (2) is applied to a body with known boundaries S_B , as shown in Fig.4. Applying Green's theorem, a general solution can be

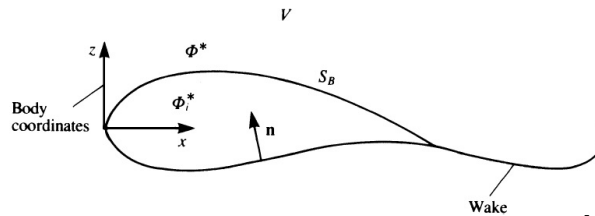


Figure 4: Potential flow over a closed body [16]

found by a sum of singularities, such as sources (σ) and doublets (μ) placed on the S_B boundary,

$$\Phi^*(x, y, z) = \frac{1}{4\pi} \int_{body+wake} \mu \mathbf{n} \cdot \nabla \left(\frac{1}{r} \right) dS - \frac{1}{4\pi} \int_{body} \sigma \left(\frac{1}{r} \right) dS + \Phi_\infty, \quad (3)$$

where r is the distance to a point outside the S_B boundary and vector \mathbf{n} points in the direction of potential jump μ . Dirichlet boundary conditions are used, which implies that the perturbation potential Φ is specified on the entire S_B surface.

The potential flow Eq.(2) does not include time dependent terms directly and, given aeroelasticity is an unsteady problem, these must be introduced through the boundary conditions. Considering a constant flow of speed U_∞ in the positive x direction, as shown in Fig. 5, a translation is applied to the body frame of reference as $(X_0, Y_0, Z_0) = (-U_\infty t, 0, 0)$ for each time step.

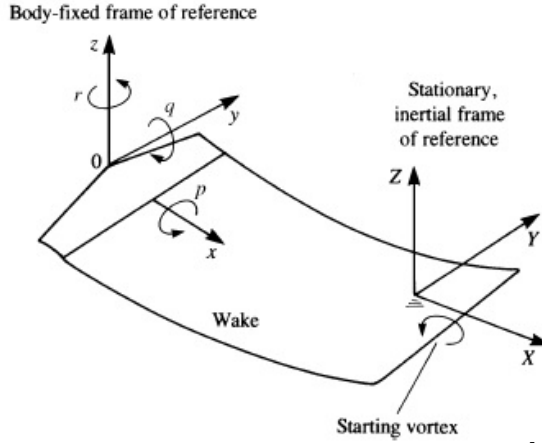


Figure 5: Inertial and body coordinates [16]

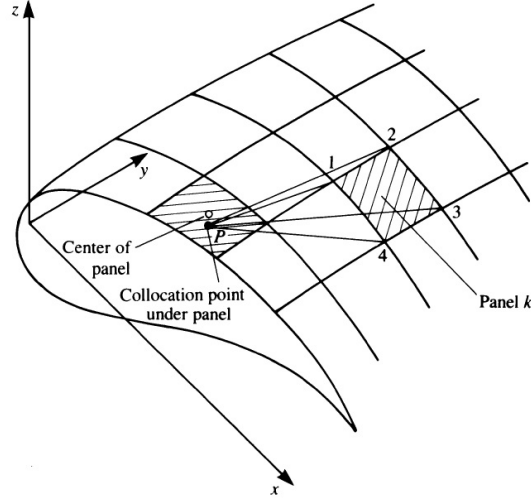
An important definition that affects the accuracy of the method is the wake geometry. A straight wake convected at the flow incidence angle was selected, as it requires fewer wake panels to be defined, decreasing significantly the computational cost, though with penalty of aerodynamic forces overestimation [16] that means dynamic instabilities will appear earlier in the simulations compared to the experiments. The body translation is used to define the new wake panel, with one extremity on the previous wake panel and the other at a X_0 distance from the other extremity, so any motion of the wing will then translate into the new wake panels.

With the boundary conditions inserted and defining the source strength as

$$\sigma = -\mathbf{n} \cdot (\mathbf{V}_0 + \mathbf{v}_{rel} + \mathbf{\Omega} \times \mathbf{r}), \quad (4)$$

where $\mathbf{V}_0 = (\dot{X}_0, \dot{Y}_0, \dot{Z}_0)$ is the velocity of the (x, y, z) system's origin, $\mathbf{v}_{rel} = (\dot{x}, \dot{y}, \dot{z})$ is the relative velocity of the body fixed frame of reference, $\mathbf{\Omega}$ is the rate of rotation of the body's frame of reference, as shown in Fig.5, and \mathbf{r} is the position vector, the problem is reduced to a set of algebraic equations with the doublet distribution μ as the unknowns.

The body's surface is discretized into N panels and the wake in N_W panels, with collocation points P at the panel center and panel vertices 1, 2, 3, 4, as shown in Fig. 6 for


 Figure 6: Influence of panel k on point P [16]

a panel k . Assuming constant source strength σ and doublet strength μ for each panel, and Eq.(2) can be rewritten as

$$\sum_{k=1}^N C_k \mu_k + \sum_{l=1}^{N_W} C_l \mu_l + \sum_{k=1}^N B_k \sigma_k = 0 \quad \text{for each internal point } P, \quad (5)$$

with

$$C_k = \frac{1}{4\pi} \int_{1,2,3,4} \frac{\delta}{\delta n} \left(\frac{1}{r} \right) dS \Big|_k \quad \text{and} \quad B_k = -\frac{1}{4\pi} \int_{1,2,3,4} \left(\frac{1}{r} \right) dS \Big|_k. \quad (6)$$

By using the Kutta condition, the wake doublets μ_l can be defined in terms of the unknown surface doublets μ_k , leading to a linear algebraic system of N equation containing N unknown singularity variables μ_k .

After solving Eq.(5) for the surface doublets μ_k , the velocity components can be evaluated numerically as

$$v_l = -\frac{\delta \mu}{\delta l}, \quad v_m = -\frac{\delta \mu}{\delta m}, \quad v_n = -\sigma, \quad (7)$$

using central differences, at panel coordinates (l, m, n) as shown in Fig. 7, These perturba-

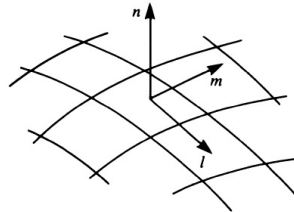


Figure 7: Panel coordinate system [16]

tion velocities are then related with the local velocity by $V_k = (U_{\infty_l} U_{\infty_m} U_{\infty_n}) + (v_l, v_m, v_n)_k$.

By defining the local velocity on each panel, the pressure coefficient C_p can be computed on a panel basis as

$$C_{p_k} = 1 - \frac{V_k^2}{U_\infty^2} - \frac{2}{U_\infty^2} \frac{\delta\phi}{\delta t}. \quad (8)$$

The pressure coefficient at time $t + \Delta t$ is computed using the Backward Euler method [17], yielding

$$C_{p_k}^{t+\Delta t} = 1 - \frac{V_{t+\Delta t}^2}{U_\infty^2} - \frac{2}{U_\infty^2} \frac{\phi^{t+\Delta t} - \phi^t}{\Delta t}. \quad (9)$$

The main advantage of using a Backward Euler method is that it is an implicit scheme, making the solution unconditionally stable, thus enabling the use of large time steps [18]. Finally, the aerodynamic force F_k for each panel is given by

$$F_k = -C_{p_k} q_\infty S_k, \quad (10)$$

where S_k is the panel area and q_∞ is the dynamic pressure.

The implementation of the 3D unsteady panel method was verified against the open-source software XFLR-5 [19] in steady mode. A rectangular wing with NACA0015 airfoil, 1.5 m span and 0.25 m chord, operating at $U_\infty=7$ m/s with 4° angle-of-attack. The discretization used an uniform mesh with 4000 panels, 100 in the chordwise direction and 40 in the spanwise direction, as shown in Fig.8. These wing dimensions match those used for the aeroelastic experimental and numerical studies.

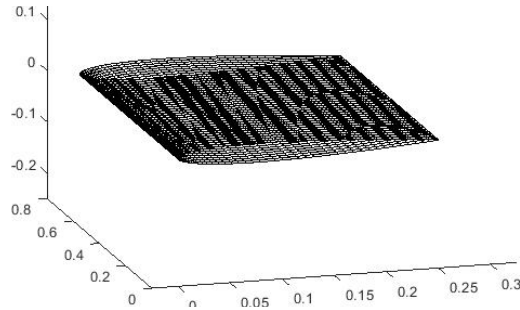


Figure 8: Aerodynamic computational mesh

The verification results, shown in Tab.1, reveal that, while the lift and pitching moment coefficients exhibit a very good match between both softwares, the drag coefficient shows a 15% disparity. Most likely, this is due to the wake shape handling [16] as both models were inviscid but, since the drag force is not very relevant in the aeroelastic response of a wing, this disparity can be found irrelevant.

3.2 Structural Model

Two types of wing sections are supported, solid and hollow, as shown in Fig. 9.

Excluding the damping effects in the fundamental Eq.(1), due to the difficulty of estimating it theoretically, Eq.(1) can be put as an eigenvalue problem,

	Aeroelastic framework	XFLR-5	difference
C_L	0.3071	0.3137	2.1 %
C_D	0.00443	0.00517	14.3 %
C_M	-0.07285	-0.07506	2.9 %

Table 1: Verification of aerodynamic coefficients

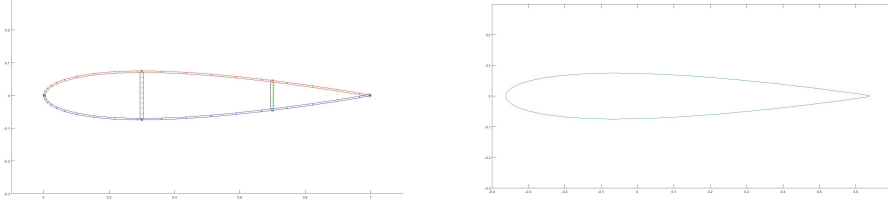


Figure 9: Hollow and solid wing sections

$$([M] - \omega^2[K])\mathbf{x} = 0, \quad (11)$$

where ω is the system frequencies, which allow for a prediction of the wing aeroelastic behavior and also to adjust the ideal time step in the unsteady calculations according to the Nyquist-Shannon sampling theorem [20],

$$t_s = \frac{1}{f_{max}}, \quad (12)$$

where f_{max} is the maximum frequency that is to be observed by the structural solver.

It should be pointed that a damped system displays divergent behavior for higher airspeeds than an undamped system so the divergence speed will be underestimated.

The 3D beam finite element implementation implied a discretization of the wing in spanwise sections, that matched those of the aerodynamic model to facilitate the FSI. The wing geometric properties and aerodynamic forces are assessed on those sections.

The selected 3D beam element is based on the Euler-Bernoulli beam theory [21], and combines the stiffness constants of a beam under the pure buckling condition $[k_b]$, a torsion bar element under pure torsion $[k_t]$ and a truss element under pure axial loads $[k_a]$, given as

$$[k_b] = \frac{EI_z}{L^3} \begin{bmatrix} 12 & 6L & -12 & 6L \\ 6L & 4L^2 & -6L & 2L^2 \\ -12 & -6L & 12 & -6L \\ 6L & 2L^2 & -6L & 4L^2 \end{bmatrix} \quad [k_t] = \frac{GJ}{L} \begin{bmatrix} 1 & -1 \\ -1 & 1 \end{bmatrix} \quad [k_a] = \frac{AE}{L} \begin{bmatrix} 1 & -1 \\ -1 & 1 \end{bmatrix} \quad (13)$$

considering the nodal displacement vectors $\mathbf{u}_b = \{v_1 \theta_{z1} v_2 \theta_{z2}\}$, $\mathbf{u}_t = \{\theta_{x1} \theta_{x2}\}$ and $\mathbf{u}_a = \{u_1 u_2\}$, for a beam of length L , elastic modulus E , shear modulus G , cross-sectional area A and cross-sectional torsion constant J ,

The representation of the 6-DOF beam element is made by the superimposition of a beam element under bending condition, a torsional bar, and a truss element, as shown in Fig.10. The global stiffness matrix $[K]$ results from the assembly of the local beam

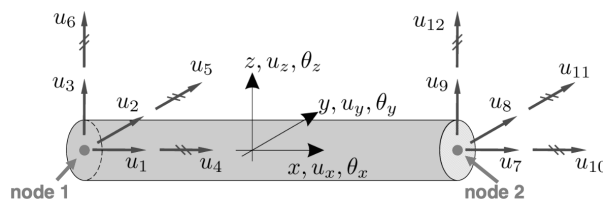


Figure 10: 3D beam element [22]

stiffness matrices $[k_e]$, after transformed from the local reference frame to the global reference frame.

To implement the dynamic structural response, a Newmark - β time integration scheme was chosen [23] as, with careful selection of parameters, the method is implicit and unconditionally stable, and so the time step can be chosen freely. The time integration procedure comprised six steps:

1. Define first acceleration estimation $\ddot{x}^i = M^{-1}(F - K x^i)$;
2. Define Newmark time integration parameters $\beta = 0.5$, $\gamma = 0.25$ and time step Δt ;
3. Calculate integration constants: $a_0 = \frac{1}{\beta\Delta t^2}$, $a_1 = \frac{1}{\beta\Delta t}$, $a_2 = \frac{1}{2\beta} - 1$, $a_3 = \Delta t(1 - \gamma)$ and $a_4 = \gamma\Delta t$;
4. Obtain effective stiffness matrix $K_{eff} = K + a_0M$;
5. Define R_{eff} matrix $R_{eff}^{i+1} = F + M(a_0x^i + a_1\dot{x}^i + a_2\ddot{x}^i)$;
6. Find displacement, velocity and acceleration values for next time-step: $x^{i+1} = K_{eff}^{-1}R_{eff}^{i+1}$, $\ddot{x}^{i+1} = a_0(x^{i+1} - x^i) - a_1\dot{x}^i - a_2\ddot{x}^i$ and $\dot{x}^{i+1} = \dot{x}^i + a_3\ddot{x}^i + a_4\ddot{x}^{i+1}$.

3.3 Fluid-Structure Interaction

The interface between aerodynamic and structural solvers uses closely coupled approach, that was made simpler by the fact that both solvers use a Lagrangian frame of reference. The implemented interface model comprises four main steps:

1. Wing displacements are determined by the structural solver using the force and moment field from the aerodynamic module at $t = N$;
2. From the displacements and mass and stiffness matrices, the structure's velocities and accelerations are computed using the Newmark - β time integration scheme;
3. Using the structures dynamic behavior, the mesh is changed using one of four interface algorithms (described next);
4. Finally, a 3D rigid body transformation is applied to the body to update the aerodynamic solver mesh for computations at $t = N + 1$.

The four interface algorithms include the Conventional Serial Staggered Algorithm (CSS1), the Serial Staggered Algorithm with First Order Structural Predictor (CSS2), the Serial Staggered Algorithm with Second Order Structural Predictor (CSS3) and an

Algorithm	Displacement calculation
<i>CSS1</i>	$x_{n+1} = u(n)$
<i>CSS2</i>	$x_{n+1} = u(n) + \Delta t v(n)$
<i>CSS3</i>	$x_{n+1} = u(n) + \Delta t(1.5v(n) - 0.5v(n - 1))$
<i>CSS4</i>	$x_{n+1} = u(n) + \frac{\Delta t}{2}v(n)$

Table 2: FSI algorithms for displacement estimation

Improved Serial Staggered Algorithm (*CSS4*). These estimate the new CFD mesh points in different manners, as shown in Tab. 2:

The effect of these algorithms on flutter speed computation were studied using the test wing geometry described in Sec. 3.1 and extruded polystyrene foam ($E=23.92$ MPa, $G=9.14$ MPa, $\rho=31.453$ kg/m³). The corresponding predicted flutter speeds were 16.66 m/s, 17.35 m/s, 16.25 m/s and 18.14 m/s. Given the proximity of these values, the fact that the Newmark- β time integration scheme does not provide very accurate velocities and accelerations, and that *CSS1* displayed the best aeroelastic behavior transition from a non-flutter condition to a flutter condition, this was the preferred algorithm.

3.4 Framework Architecture

The aeroelastic framework was developed with three goals in mind: user-friendly to debug and produce results; reusability to allow for modules to be easily exchanged or added; and low maintenance to reduce the time required to check connections between modules. This led to a modular framework with clearly separated aerodynamic and structural modules, as schematically seen in Fig. 11. These included:

- steady aerodynamic module: defines initial aerodynamic mesh and starts aerodynamic computations at $t = 0$;
- unsteady aerodynamic module: performs aerodynamic computations for any $t > 0$,
- structural module: defines structural mesh, computes mass and stiffness matrices, and nodal forces;
- Newmark module: performs structural time integration from time t to $t + \Delta t$;
- Fluid-Structure Interaction module: couples the aerodynamic and structural modules and advances the aerodynamic mesh from t to $t + \Delta t$.

An analysis was made for the computing time for a case with 300 iterations, using a computer with an Intel[®] Core[™] i7-2630QM with 8Gb of RAM, and the timings for each module are listed in Tab. 3. Most of the computing time is spent on the fluid solver module due to the calculation of the aerodynamic influence coefficients matrix, as each panel must be compared to every other panel in the wing for each time iteration.

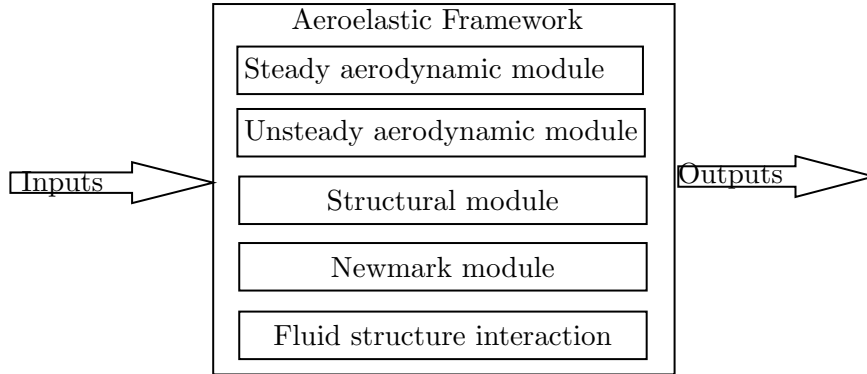


Figure 11: Modular aeroelastic framework architecture

Module	Time (s)
Fluid solver	1403.6
Structural solver and time integration	3.3
Fluid structure interaction	1.5
Other sources	0.9
Total	1409.3

Table 3: CPU time per aeroelastic framework module

4 NUMERICAL RESULTS

4.1 Problem Description

The objective is to perform numerical and experimental dynamic aeroelastic analyses on a simple rectangular wing. To do so, a baseline wing with airfoil NACA 0015 made of extruded polystyrene rigid foam is used, with properties shown in Tab.4.

Fluid and structural solver options		Wing geometric properties	
Time step	0.005 s	Airfoil	NACA 0015
Total time	1.5 s	Half span	0.75 m
FSI algorithm	CSS1	Root chord	0.25 m
Structural subiterations	0	Taper ratio	1
		Sweep angle	0°
		Dihedral angle	0°
		Angle of attack	4°
Material properties		Flight conditions	
Young's modulus	23.92 MPa	Freestream velocity	10.0 m/s
Shear modulus	9.14 MPa	Altitude	0 m
Material density	31.453 kg/m ³	Air density	1.225 kg/m ³

Table 4: Baseline numerical wing test case parameters

Before the aeroelastic analysis design was started, a modal analysis was performed, using the aeroelastic framework developed using Eq.(11). The first 8 frequencies are shown in Tab.5. With the definition of the wing natural vibration frequencies and considering

Mode	Frequency (Hz)	Mode	Frequency (Hz)
1 st flapwise bending	7.9	2 nd torsion	176.8
2 nd flapwise bending	48.4	1 st chordwise bending	244.2
1 st torsion	58.9	4 th flapwise bending	248.0
3 rd flapwise bending	132.2	5 th flapwise bending	291.4

Table 5: Modes and natural frequencies of tested wing

that time step values lower than 0.005 s are not feasible to use due to program constraints, the time step chosen is the lowest value possible. This time step allows to capture both flapwise bending and torsion modes, which were shown to be the major components in achieving divergent behavior.

4.2 Grid Convergence Study

A convergence study was conducted to assess the required number of chordwise nc and spanwise ns points. The wing test case parameters are summarized in Tab.4.

The aerodynamic forces are the output parameters used in the convergence study since they are the primary source of wing loading, in particular the lift component. To select the most appropriate mesh for the aeroelastic analysis, the aerodynamic coefficients were computed using four different meshes, and the results are shown in Tab.6.

Mesh $nc \times ns$	20×10	40×20	64×30	100×40
C_L	0.2947	0.3041	0.3075	0.3092
C_D	0.0101	0.0060	0.0044	0.0032
Computing time	0.30 s	1.29 s	6.32 s	26.48 s

Table 6: Grid convergence test

While the number of chordwise points affects mainly the aerodynamic component, the spanwise points also affect the structural module. As such, ns should not be lower than 10 points. By checking the aerodynamic coefficients, there is a low variation of the lift coefficient but coarser meshes grossly overestimates the induced drag. Another important value is the computational time, as the value shown is for only one aerodynamic iteration, but each numerical aeroelastic test performed is expected to require more than 300 iterations per freestream velocity. Therefore, the mesh that presents the best trade-off between accuracy and computational cost is the 40×20 mesh.

Another study was conducted to assess the wing tip displacement variation with the number of panels, resulting in the roughly the same conclusion about mesh size.

4.3 Flutter Speed Estimation

Since most structural vibration phenomena can be characterized as a damped harmonic motion, the damping ratio g was estimated to find the flutter speed, defined as the threshold between dynamic stability and instability, that is, the transition from positive to negative damping ratio [24].

The damping ratio ζ can be obtained from the logarithmic increment [12], defined as

$$\delta_n = \frac{1}{n} \ln \frac{X_i}{X_{i+n}} = \frac{2\pi\zeta}{\sqrt{1-\zeta^2}}. \quad (14)$$

The damping ratio computed for a number of freestream velocities is shown in Fig.12(bottom) using the parameters in Tab.4. In addition, a Fast-Fourier transform (FFT) is performed on the corresponding wing tip displacement behavior to check the frequency evolution with the increase in velocity, also shown in Fig.12(top).

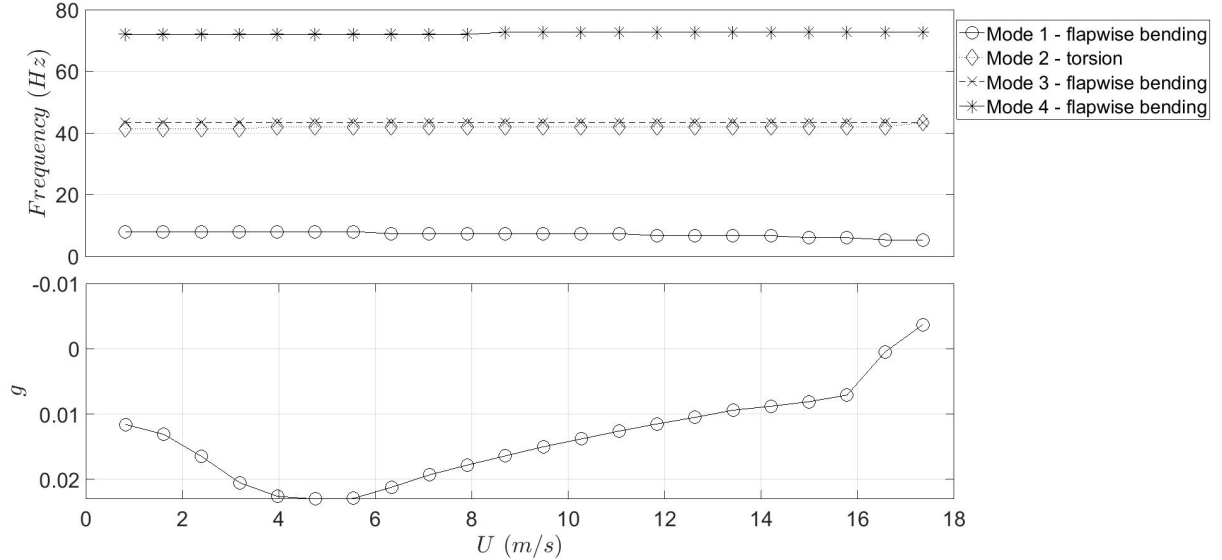


Figure 12: f-U and U-g graphs for the baseline numerical case

The flutter speed, corresponding to the transition from a positive to a negative damping ratio, occurs at $U=16.66$ m/s for the simulated wing. The null damping ratio is considered the primary method to find the flutter speed but, by analyzing the frequency spectra, an approximate estimation can also be found by checking when two separate frequencies coalesce into a single value. As shown in Fig.12(top), vibration modes 2 (torsion) and 3 (bending) have the same frequency for a velocity of 17.35 m/s, implying that the wing is experiencing divergent behavior.

4.4 Flutter Speed Index Comparison

The Flutter Speed Index [5] is defined as

$$U_f = \frac{U_\infty}{b\omega_a\sqrt{\mu}}, \quad (15)$$

where U_∞ is the freestream velocity, b is the wing span, ω_a is the first torsional mode frequency and μ is the mass ratio of the wing [5]. The definition of the mass ratio of the wing comes from stability theory [25], $\mu = m / \frac{1}{2} \rho_{air} S \bar{c}$, where m is the wing mass, ρ_{air} is the air density, S the aerodynamic wing area and \bar{c} the mean chord of the wing.

A comparison between the flutter speed index obtained for the numerical analysis and an experimental test is shown in Fig. 14. The baseline wing corresponds to the one simulated in Sec.4.3, while the reduced span wing has a half-span of 0.625 m.

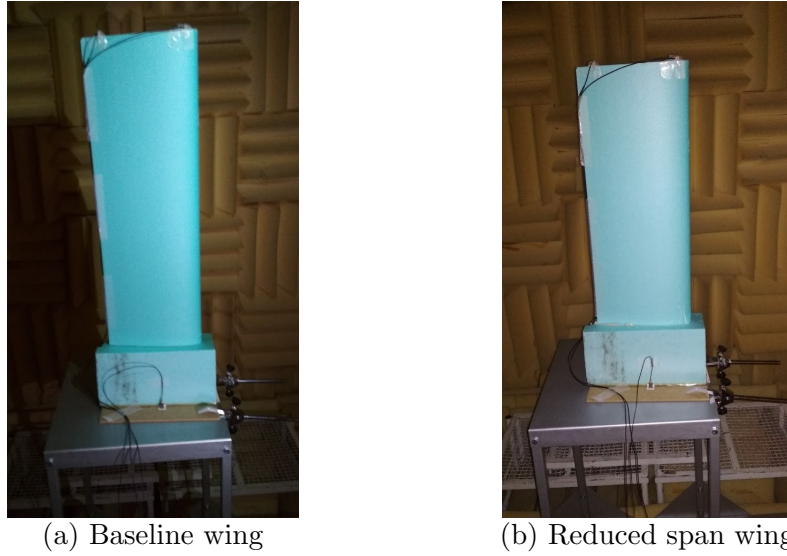


Figure 13: Experimental wing models

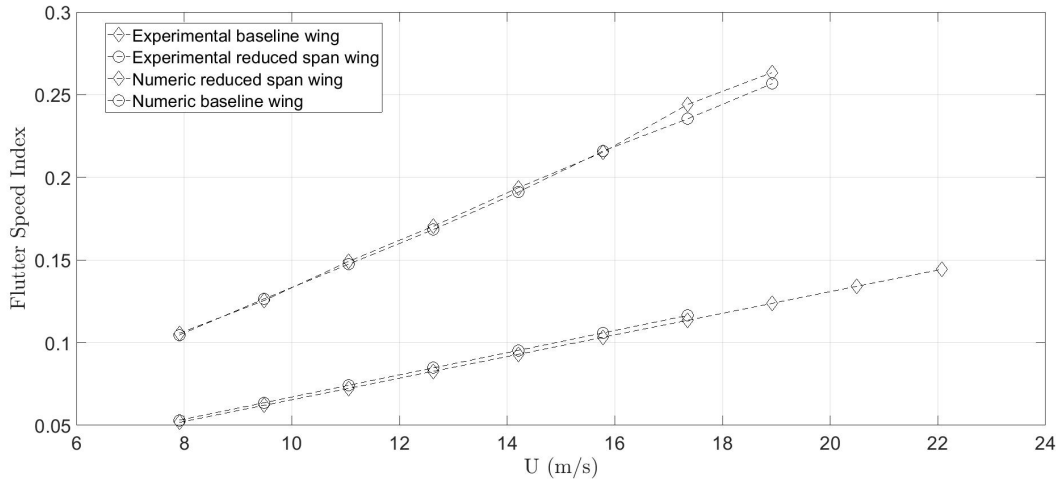


Figure 14: Flutter Speed Index variation with freestream velocity

For both the experimental and the numerical cases, the flutter speed index remains close between the two wings, despite having different span and torsional behavior.

The major difference occurs between the experimental and numerical results, that is attributed to the difference in the first torsional mode observed, as all other parameters are

equal. The disparities can be explained by the overestimation of aerodynamic forces and the lack of damping in the numerical model, and by parasite vibrations of the experimental wing mount model that contribute to the damping of the wing natural vibrations.

Also worth noting that, for the numerical case, no values of the flutter speed index are computed on the baseline wing for a velocity greater than 17.35 m/s due to the presence of highly divergent behavior of the wing, consistent with the expected post-flutter.

4.5 Flutter Speed Sensitivity to Wing Aspect Ratio

As the experimental testing showed, there is a significant change in the wing's aeroelastic behavior with aspect ratio, mainly due to the increase in wing rigidity. To further study the variation of aeroelastic behavior, a parametric sensitivity analysis of the wing flutter speed with respect to its aspect ratio was performed using the numerical model developed.

The wing defined in Tab.4 was used but letting the span vary so that the aspect ratio ($AR = b/\bar{c}$) ranged between 4 and 7.6. The numerical results obtained are shown in Fig.15.

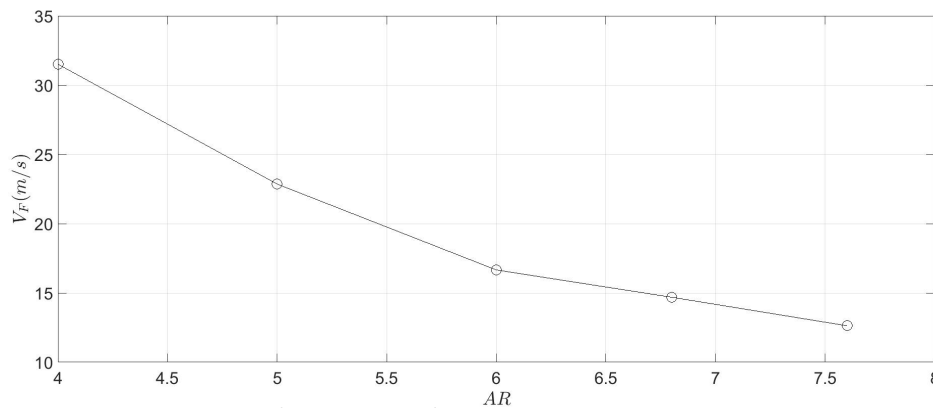


Figure 15: Flutter speed sensitivity to wing aspect ratio

As expected, there is an increase of the flutter speed with the decrease of the wing aspect ratio, effectively doubling its value for aspect ratio values between 4 and 6, while the evolution for values greater than 6 is lower, thus exhibiting an inversely quadratic dependence with aspect ratio. Aspect ratios greater than 8 were not computed since the developed numerical code still does not account for non-linear geometric or displacement behaviors. The increase of flutter speed by decreasing the aspect ratio is mainly due to the increase of the wing rigidity.

4.6 Static Aerodynamic Optimization

The first optimization problem pursued was a purely aerodynamic design problem for maximum lift-to-drag ratio, with constraints in lift coefficient and wing area to assure that the optimized wings produce the same lift as the baseline. The baseline wing geometry and operating conditions were the same as in Tab.4.

The numerical analyses were conducted with the static aerodynamic solver incorporated in the aeroelastic framework, and the constrained optimization algorithm SQP in function *fmincon* in MATLAB[®] was used to solve the problem cast in the form

$$\begin{aligned}
& \text{Maximize} && L/D \\
& \text{with respect to} && \mathbf{x} \\
& \text{subject to} && S \geq 0.375 \text{ m}^2 \\
& && C_L \geq 0.3 \\
& && 1.3 \leq b \leq 1.7 \text{ m} \\
& && 0.25 \text{ m} \leq c_{root} \leq 0.4 \text{ m} \\
& && \lambda \geq 0.4 \\
& && -5^\circ \leq \theta_{root}, \theta_{tip} \leq 5^\circ,
\end{aligned} \tag{16}$$

where the wing design variables vector \mathbf{x} included the half span $b/2$, root chord c_{root} , taper ratio λ , root twist angle θ_{root} and tip twist angle θ_{tip} .

Since only the static aerodynamic solver was used in the analysis, the finer mesh in Tab.6 with 100 chordwise points and 40 spanwise points was used

The objective function, design parameters and corresponding bounds, and the constraints are shown in Tab.7, for both the baseline and optimized wing. The optimizer

		Baseline Wing	Optimized wing
Lift-to-drag ratio	L/D	96.78	178.89
Half span	$b/2$	0.75 m	0.85 m
Root chord	c_{root}	0.25 m	0.3162 m
Taper ratio	λ	1.0	0.4
Root twist	θ_{root}	0°	-0.9883°
Tip twist	θ_{tip}	0°	1.1472°
Area	S	0.375 m ²	0.3762 m ²
Mass	m	0.1510 kg	0.1452 kg
Lift coefficient	C_L	0.3097	0.3006
Drag coefficient	C_D	0.0032	0.0017
Pitch coefficient	C_M	-0.0738	-0.0782

Table 7: Static wing aerodynamic optimization

satisfied all constraints and, while there wing lift coefficient remained almost constant, the drag coefficient decreased, thus leading to the desired increase in lift-to-drag ratio. This resulted from an optimal wing taper ratio that led to an approximately elliptical lift distribution, thus reducing the induced drag. The final wing shape is shown in Fig.16.

4.7 Static Structural Optimization

The second optimization problem consisted of the minimization of the wing mass, keeping the same aerodynamic constraints and mesh as in Sec.4.6.

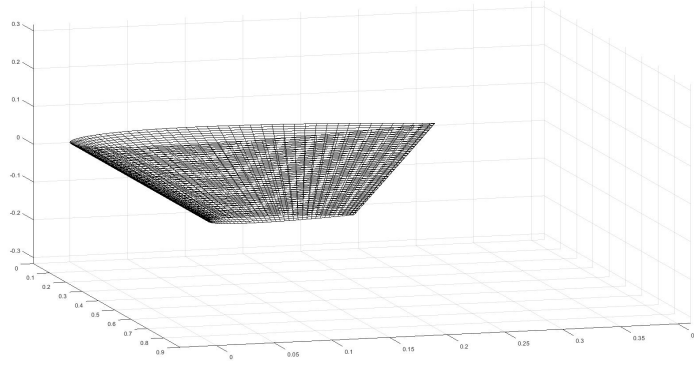


Figure 16: Wing design for static aerodynamic optimization

The objective, design parameters and constraints are summarized in Tab.8.

		Baseline wing	Optimized wing
Mass	m	0.1510 kg	0.1415 kg
Half span	$b/2$	0.75 m	0.85 m
Root chord	c_{root}	0.25 m	0.25 m
Taper ratio	λ	1.0	0.8
Root twist	θ_{root}	0°	-0.1658°
Tip twist	θ_{tip}	0°	-0.3749°
Area	S	0.375 m^2	0.3826 m^2
Lift coefficient	C_L	0.31	0.30
Lift-to-drag ratio	L/D	96.78	142.49

Table 8: Static structural wing optimization

Since the final mass is marginally smaller than in the previous case, and considering the difference in L/D , the wing from the aerodynamic optimization case is preferred over this from a design perspective.

4.8 Flutter Speed Optimization

In this optimization problem, a function was defined to determine the freestream speed for which the numerical aeroelastic solver achieves a divergent oscillatory solution, which was identified as the flutter speed. Due to the added computational cost of the unsteady analyses, the coarse mesh of 40×20 panels presented in Sec.4.2 was used.

The constraints are mostly the same as stated in Sec.4.6, excluding the speed constraint

that is not applicable. The wing flutter optimization problem can then be cast in the form

$$\begin{aligned}
 & \text{Maximize} && U_{flutter} \\
 & \text{with respect to} && \mathbf{x} \\
 & \text{subject to} && C_L \geq 0.3 \\
 & && 1.3 \leq b \leq 1.7 \text{ m} \\
 & && 0.25 \text{ m} \leq c_{root} \leq 0.4 \text{ m} \\
 & && \lambda \geq 0.4 \\
 & && -5^\circ \leq \theta_{root}, \theta_{tip} \leq 5^\circ,
 \end{aligned} \tag{17}$$

The parameters of the optimal wing obtained are listed in Tab.9.

		Baseline wing	Optimized wing
Flutter speed	$U_{flutter}$	16.66 m/s	28.56 m/s
Half span	$b/2$	0.75 m	0.85 m
Root chord	c_{root}	0.25 m	0.4 m
Taper ratio	λ	1.0	0.5848
Root twist	θ_{root}	0°	0°
Tip twist	θ_{tip}	0°	5°
Area	S	0.375 m ²	0.3762 m ²
Mass	m	0.1510 kg	0.1452 kg
Lift coefficient	C_L	0.31	0.46

Table 9: Flutter speed optimization

The optimized wing achieved a large increase in flutter speed compared to the baseline wing, while also maintaining a low mass and a greater base C_L , in part due to the increase in taper ratio and large wing tip twist.

5 CONCLUSIONS

A modular numerical aeroelastic framework was implemented in MATLAB[®] to reduced program complexity and facilitate future add-ons or replacements of existing modules. The aerodynamic module was verified against open source software XFLR-5 and the structural module accuracy compared to ANSYS[®].

The numerical framework was shown to be able to estimate the flutter speed both by computing the damping ratio associated to the wing's dynamic behavior and the structural frequency spectra that results from this dynamic behavior.

The comparison of numerical and experimental data showed a discrepancy between the measured frequency spectra for both cases, with the experimental results displaying a higher rigidity comparing to numerical results. While this variation cannot be dismissed, it can be seen as an extra safety margin since the numerical model underestimates the wing flutter speed and thus experimental tests can be performed within safety limits.

The effect of the wing aspect ratio on the flutter speed was studied, which showed that the wing bending rigidity plays a crucial role on the aeroelastic instabilities and further illustrating the major design challenge of increasing the aspect ratio to improve the lift-to-drag ratio.

The optimization test cases served as another illustration of the aeroelastic framework versatility and also verify the results that were well within expectation for the static aerodynamic and structural cases, and the dynamic aeroelastic final case.

ACKNOWLEDGEMENTS

This work was supported by FCT (Foundation for Science and Technology) through ID-MEC (Institute of Mechanical Engineering), under LAETA project UID/EMS/50022/2019.

REFERENCES

- [1] Edmund W. Pendleton, Denis Bessette, Peter B. Field, Gerald D. Miller, and Kenneth E. Griffin. Active aeroelastic wing flight research program: Technical program and model analytical development. *Journal of Aircraft*, 37:554–561, August 2000. DOI:10.2514/2.1484.
- [2] Gerald Andersen, David Cowan, and David Piatak. Aeroelastic modeling, analysis and testing of a morphing wing structure. In *48th AIAA/ASME/ASCE/AHS/ASC Structures, Structural Dynamics, and Materials Conference*, page 1734, 2007.
- [3] Frank H. Gern, Daniel J. Inman, and Rakesh K. Kapania. Structural and aeroelastic modeling of general planform wings with morphing airfoils. *AIAA Journal*, 40:628–637, April 2002. DOI:10.2514/2.1719.
- [4] W. E. Silva and R. E. Bartels. Development of reduced-order models for aeroelastic analysis and flutter prediction using the CFL3Dv6.0 code. *Journal of Fluids and Structures*, 19:729–745, March 2004.
- [5] Ramji Kamakoti and Wei Shyy. Fluid-structure interaction for aeroelastic applications. *Progress in Aerospace Sciences*, 40:535–558, November 2004. DOI:10.1016/j.paerosci.2005.01.001.
- [6] Ryan J Beaubien, Fred Nitzsche, and Daniel Feszty. Time and frequency domain flutter solutions for the AGARD 445.6 wing. 2005.
- [7] M. Kämpchen, A. Dafnis, H.-G. Reimerdes, G. Britten, and J. Ballman. Dynamic aero-structural response of an elastic wing model. *Journal of Fluids and Structures*, 18:63–77, July 2003.
- [8] Robert Bennett and John Edwards. An overview of recent developments in computational aeroelasticity. In *29th AIAA, Fluid Dynamics Conference*, page 2421, 1998.
- [9] Earl Dowell, John Edwards, and Thomas W. Strganac. Non-linear aeroelasticity. *Journal of Aircraft*, 40:857–874, October 2003. DOI:10.2514/2.6876.
- [10] Deman Tang and Earl H Dowell. Experimental and theoretical study on aeroelastic response of high aspect-ratio wings. *AIAA Journal*, 39:1430–1441, August 2001. DOI:10.2514/2.1484.
- [11] Earl H Dowell and Kenneth C Hall. Modelling of fluid-structure interaction. *Annual Review of Fluid Mechanics*, 2001.
- [12] Singiresu S. Rao. *Mechanical Vibrations*. Prentice Hall, 5th edition, 2011. ISBN:978-0-13-212819-3.

- [13] Frederico Afonso, José Vale, Éder Oliveira, Fernando Lau, and Afzal Suleman. A review on non-linear aeroelasticity of high aspect-ratio wings. *Progress in Aerospace Sciences*, 89:40–57, February 2017.
- [14] Brian Maskew. Program VSAERO theory document: a computer program for calculating nonlinear aerodynamic characteristics of arbitrary configurations. *NASA CR 4023*, September 1987.
- [15] J. N. Reddy. *An Introduction to the Finite Element Method*. McGraw-Hill, 3rd edition, 2010. ISBN:007-124473-5.
- [16] Joseph Katz and Allen Plotkin. *Low Speed Aerodynamics*. Cambridge University Press, 2nd edition, 2001. ISBN:978-0-521-66219-0.
- [17] J. H. Ferziger and M. Peric. *Computational Methods for Fluid Dynamics*. Springer, 3rd edition, 2002. ISBN:978-3-540-42074-3.
- [18] Charles Hirsch. *Numerical computation of internal and external flows: The fundamentals of computational fluid dynamics*. Elsevier, 2nd edition, 2007. ISBN:978-0080550022.
- [19] Mark Drela, Harold Youngren, M. Scherrer, and A. Deperrois. XFLR 5, 2012.
- [20] Abhishek Yadav. *Analog Communication System*. Firewall Media, 1st edition, 2008. ISBN:978-8131803196.
- [21] O.A. Bauchau and J.I. Craig. Euler–Bernoulli beam theory. In *Structural analysis*, pages 173–221. Springer, 2009.
- [22] Jo ao Almeida. Structural dynamics for aeroelastic analysis. Master’s thesis, Instituto Superior Técnico, Universidade de Lisboa, November 2015.
- [23] Leigh William and Mario Paz. *Structural Dynamics: Theory and Computation*. Springer, 5th edition, 2012. ISBN:978-1461504818.
- [24] Dewey H. Hodges and G. Alvin Pierce. *Introduction to Structural Dynamics and Aeroelasticity*. Cambridge University Press, 2nd edition, 2011. ISBN:978-0-521-19590-4.
- [25] Bernard Etkin and Lloyd Duff Reid. *Dynamics of Flight: Stability and Control*. Wiley, 3rd edition, 1995. ISBN:978-0471034186.